Online Health Monitoring of Silicon PV Panels by Converter-Based Impedance Spectroscopy: Panel-Level Equivalent Circuit Model & Health Feature Extraction

Xin Wang, *Student Member, IEEE,* Zhixue Zheng, *Member, IEEE,* Michel Aillerie, Marie-Cécile Péra, Daniel Hissel, *Fellow, IEEE*

***Abstract*—Converter-based impedance spectroscopy (IS) provides a promising tool to achieve online health monitoring of photovoltaic (PV) panels without additional equipment. However, to obtain a relatively complete IS spectrum of the PV panel, the frequency of the perturbation signal should reach at least 100 kHz, posing a great challenge for the current switching and sampling devices of power converters. Meanwhile, to correctly and clearly interpret the internal physical processes of the PV panel based on IS measurements, establishing an appropriate AC equivalent circuit model (AC-ECM) is essential. Nowadays, the existing AC-ECMs in PV domain are generally at the cell level, which exhibit inherent complexity for online implementation at the panel level. Moreover, the effect of bypass diodes is typically ignored, which affects the analysis under faulty conditions, such as partial shading. To address these issues, this work aims to propose a systematic health monitoring methodology for PV panels by converter-based IS. Firstly, an appropriate panel-level AC-ECM is established by both simplifying the internal relaxation processes at the cell level and considering the existence of bypass diodes. Secondly, the proposed AC-ECM enables fitting the measured IS spectra over a lower frequency range of [1 Hz, 2 kHz], efficiently responding to variations in environmental conditions. Thirdly, four health features are originally defined and extracted based on the proposed AC-ECM, including $\ln(R_p)/V_{PV}$, $\ln(C_p)/V_{PV}$ to analyze the influence of temperature and output voltage, R_s + R_p to reflect the PV panel's conductivity, and τ to describe the recombination process. Experimental verification has been performed under various operating conditions, including different temperatures, irradiance levels and partial shading percentages. The results indicate that the proposed methodology can efficiently characterize the different operating conditions of the PV panel.**

***Index Terms*—AC equivalent circuit model, Converter-based impedance spectroscopy, Photovoltaic panels, Health features.**

I. Introduction

With the reduction of fossil energy and the impact of greenhouse gases, solar energy shows extremely high prospects due to its pollution-free nature and wide distribution. Photovoltaic (PV) cells can directly converts the solar energy into electricity, fulfilling a part of the energy needs of various applications in daily lives, transportation, industries and residential buildings connected by converters [1]–[3]. For example, the installation of solar energy in Europe is planned to reach nearly 600 GW by 2030 [4]. However, the annual power losses in PV generation caused by various faults are estimated to be around 18.9% [5]. Additionally, some faults may result in safety risk, such as arcs and short-circuits, which can cause fires [6]. Therefore, monitoring health states is crucial to ensuring the reliability and efficiency of the entire system. Considering the percentage of commercial products, silicon PV panels, which are the most popular devices in the PV market [7], [8], are primarily targeted in this work. In the following sections, PV cells/panels represent the silicon PV cells/panels for convenience.

Over the past decade, various health monitoring methods in the PV domain have been proposed for different applications [9], [10]. According to whether PV panels have power output during monitoring the health states, these methods can be classified into two types: offline and online methods. With offline methods, PV panels do not output power, leading to poor operating efficiency [11]–[13]. In comparison, online methods can assess the health states of the system while maintaining power output, making them more attractive to researchers, such as IV curves [14] and impedance spectroscopy (IS) measurements [15]. A detailed comparison of various characterization methods was conducted in the authors' previous work [2]. More specifically, IV curve-based methods rely on the IV curve of a PV panel, which contains DC current and voltage information. By applying data analysis techniques, the faults of PV panels can be identified. However, obtaining the IV curve requires scanning across the entire voltage range (from open-circuit to short-circuit conditions), which reduces operating efficiency and interrupts continuous power output. In comparison, IS measurement-based methods analyze the health states by injecting perturbation signals over a wide frequency range. From the perturbation and response signals, impedance information can be extracted, including insights into internal relaxation processes. A key advantage of converter-based IS measurements is that they do not require a costly workstation and can be implemented online at a

This work was supported by French national agency (ANR) project JCJC EREMITE (Grant number: ANR-19-CE05-0008-01) and Chinese Scholarship Council (Corresponding author: Zhixue Zheng).

X. Wang, Z. Zheng, M. C. Péra and D. Hissel are with the Université Marie et Louis Pasteur, UTBM, CNRS, institut FEMTO-ST, FCLAB, F-90000, Belfort, France (e-mail: xin.wang@univ-fcomte.fr; zhixue.zheng@univ-fcomte.fr; marie-cecile.pera@univ-fcomte.fr; daniel.hissel@univ-fcomte.fr), and D. Hissel is also with Institut Universitaire de France (IUF), 75005 Paris, France. M. Aillerie is with the Université de Lorraine and CentraleSupélec, LMOPS, F-57000 Metz, France (e-mail: michel.aillerie@univ-lorraine.fr).

fixed operating point, ensuring higher operating efficiency and continuous power output. However, this technique is rarely applied to PV panels, highlighting the need for an appropriate AC equivalent circuit model (AC-ECM) at the panel level, clearly defined health features and efficient fault diagnosis methods.

IS measurement is widely used in batteries, fuel cells, and materials corrosion, where it demonstrates high efficiency and accuracy [16]–[19]. IS is also employed to evaluate the internal physical information of PV cells to improve their overall performance [20]–[24]. However, most applications rely on a specific work-station. Due to its high cost and considerable volume, this tool is rarely applied to PV panels especially in small-scale applications such as residential applications.

On the other hand, the method known as converter-based IS generates the perturbation signals by controlling the duty cycle of the existing DC/DC power converters [25]–[27]. In this way, no additional equipment is required. Both cost and volume of the target system are decreased. To ensure the reliability and accuracy of IS measurements, the control method and the AC equivalent circuit model (AC-ECM) of the target system are the two main aspects of concern. Authors in [28] and [29] achieved the online IS measurements of the battery based on the bidirectional DC-DC converter and the interleaved boost/buck converter, respectively. However, the corresponding control methods are specifically designed based on the battery characteristics. In [2], three online control methods were developed based on commonly used controllers in linear system, allowing stable perturbation signals to be injected online while considering the characteristics of the PV panel, including output voltage, output current and the frequency requirements. However, the AC-ECM, composed of electrical elements, is an essential part for interpreting the health state information of PV panels based on the obtained impedance.

The fundamental physic structure of PV cells was provided in [30]. Both DC- and AC- ECMs of PV cells was proposed and analyzed in [31]. The variation in capacitance with the DC-bias voltage of the PV cell across both the quasi-linear current region [32] and the entire voltage range were revealed in [33]. Considering the influence of the illumination, an AC-ECM considering three relaxation processes was proposed in [22], with a frequency range of [1 Hz, 1 MHz]. However, applying this model in practical applications is challenging and costly due to the need to cover the entire frequency range. Additionally, to mitigate the effects of hot spots and partial shading, multiple bypass diodes are often connected within a single panel, which plays an important role in quantifying the influence of environmental factors. Directly applying the cell model for data analysis may introduce deviation, especially under partial shading conditions. A dynamic model of the PV panel was proposed in [34], and this model was used to detect the hot spots in PV panels in [35]. While this model is well suited for enhancing the IV curve performance during hardware-in-the-loop simulations of PV panels, it is not suitable for analyzing the IS data due to the variable relaxation processes of PV panels at different injection points.

To overcome these shortcomings and provide a basis for evaluating the health states of the PV panel using converter-based IS, a simplified AC-ECM at the panel level is established in this work. The influence of the operating conditions on the internal parameters is systematically studied. The major contributions are listed as follows:

- An appropriate AC-ECM at the panel level is proposed based on the relaxation processes at the cell level, while taking into account the existence of bypass diodes and the limitation imposed by converter bandwidth.
- The physical meaning of each parameter in the AC-ECM is interpreted by analyzing the internal relaxation processes. Furthermore, four health features with specific physical meanings are originally defined and extracted from the IS spectra with a limited frequency range to assess the health states of the PV panel.
- Experimental verification has been conducted under various operating conditions, including different temperatures, irradiance levels and partial shading percentages, to verify the effectiveness of the proposed AC-ECM and the defined health features.

The following sections are organized as follows. The basic operating principle of converter-based IS applied to PV panels is introduced in Section II. In Section III, a simplified AC-ECMs at the panel level is presented, taking into account the internal physical processes, the limitations of converter bandwidth, and the existence of bypass diodes. Meanwhile, four health features with specific physical meanings are defined accordingly to reflect the health states of the PV panel. Section IV provides experimental verification under different operating temperatures, irradiance levels and partial shading percentages. Section V presents the conclusions and perspectives.

II. Converter-based IS

Fig. 1 illustrates a conventional boost converter with integrated IS for a PV panel. The corresponding parameters are listed as follows: S - the power source/PV panel; i_{PV} - the output current of the PV panel; L - the filter inductor; $Diode$ - the diode of the converter; T_{sw}, d - the switch and its corresponding duty cycle; C - DC bus capacitor; R_L - the load of the system; v_{PV} - the the output voltage of the PV panel; i_{ac}, v_{ac} - AC components of the PV panel's voltage and current. Regarding the converter-based IS implementation, two parts are indicated in Fig. 1: converter control and IS post-treatment.

The converter control part achieves the cooperative control among different modes, i.e, maximum power point tracking (MPPT), injection point tracking (IPT) and IS modes, as well as the detailed control of each mode. In the authors' previous work, a systemic design guideline for the control strategy has been proposed [2]. Specifically, the unified control strategy is utilized in this work, and the corresponding control block is depicted in Fig. 2, where I_{ref-dc} and i_{ref-ac} represent the reference of DC and AC components, $G_{i_{pv}-d}(s)$ is the transfer function of the duty cycle to the output current of the PV panel by Laplace transform, and $G_{PI}(s)$ is the transfer function of the PI controller. Corresponding parameters that ensure the validity of IS measurement can be calculated based on the proposed method.

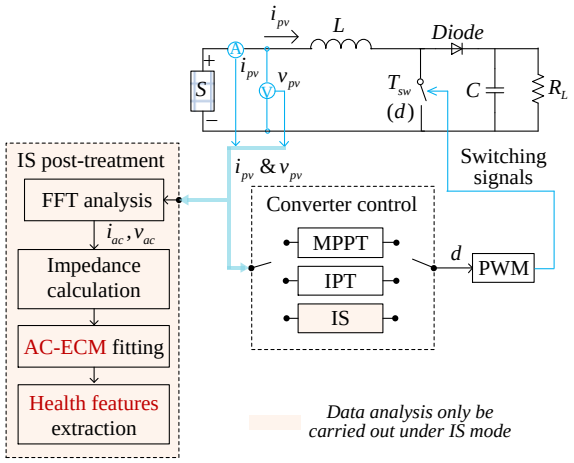

Fig. 1. Implementation of converter-based IS for the PV panel

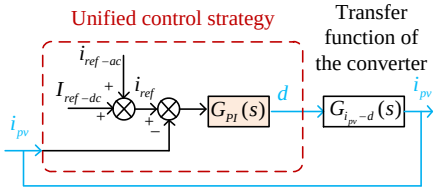

Fig. 2. Unified control strategy for converter-based IS implementation [2]

The IS post-treatment part focuses on the acquisition and treatment of impedance information in IS mode. The perturbation and response signals, i.e., i_{ac} and v_{ac}, are extracted by Fast Fourier Transform (FFT) analysis of the sampled current and voltage signals. Based on the collected signals, the PV panel's internal impedance at the injection point, i.e., $Z_{PV}(f_p)$, can be calculated as:

$$Z_{PV}(f_p) = v_{ac}(f_p)/i_{ac}(f_p) \tag{1}$$

where f_p is the frequency of the perturbation signal.

Based on the calculation results of (1), the AC-ECM fitting is then performed to extract the equivalent internal parameters. Subsequently, the health features can be defined based on the impedance information to describe the health states of the PV panel. To ensure effective health monitoring relying on the converter-based IS measurements, two major aspects in IS post-treatment part should be specifically addressed:

1) **Appropriate AC-ECM at the panel level:** The frequency range of the perturbation signal should be as wide as possible to capture all relevant information. However, the high-frequency range of perturbation and response signals is limited by switching power devices and converter control. Thus, an appropriate AC-ECM to interpret a limited frequency range, is needed.
2) **Effective health features:** Health features are used to describe the health states under various operating conditions and should be related to the internal physical processes. Since IS is rarely applied in PV panels, there is a lack of effective health features associated with the AC-ECM of PV panels.

III. AC-ECM OF THE PV PANEL

This section focuses on the AC-ECM of the PV panel by analyzing the internal relaxation processes of the PV cell while considering the existence of bypass diodes and the limitation imposed by converter bandwidth.

A. AC-ECM of the panel

A simplified physical structure of the silicon PV cell is shown in Fig. 3 (a), which mainly relies on a $p-n$ junction to achieve the conversion from solar energy to electricity. The absorbed solar energy excites the electrons in the $p-n$ junction, resulting in the formation of free electrons and holes, known as carriers. The output current and the corresponding output voltage are denoted as I_{PV} and V_{PV} respectively.

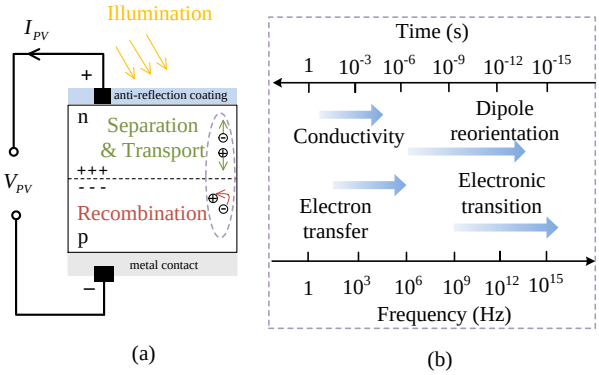

Fig. 3. Relaxation processes: (a) Simplified physical structure of the silicon PV cell; (b) Relaxation processes in silicon PV cells (adapted from [36]).

During the energy conversion, there are four main relaxation processes inside the PV cell, with the corresponding typical time scales and frequency ranges indicated in Fig. 3 (b). Based on the different time scales, these relaxation processes can be classified into: 1) femtosecond-level relaxation process, which is caused by electronic transitions and can typically be studied using transient optical spectroscopy; 2) nanosecond-level relaxation process, which describes the molecular or lattice polarization and dipolar rearrangement, which can be observed using dielectric spectroscopy; 3) microsecond-level relaxation processes, which can be investigated using electrical spectroscopy and arises from both electronic and ionic conduction as illustrated in Fig. 3 (b) in terms of conductivity and electron transfer, and are also referred to as diffusion/transition and recombination processes [22], [33], [37]. These two relaxation processes are generally equivalent to two sub-circuits and the corresponding complete impedance spectrum typically contains two arcs, as shown in Fig. 4.

According to the turning points of the IS spectrum and its intersections with the real axis, as indicated in Fig. 4, the overall frequency range can be separated into four segments:

- Low frequency range ($f_0 \leq f \leq f_1$): Based on the IS spectrum in this range, only the total resistance information can be accurately obtained.
- Medium frequency range ($f_1 \leq f \leq f_2$): When the maximum frequency of the perturbation signal can reach

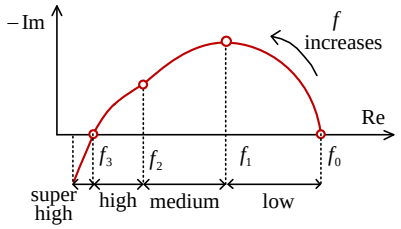

Fig. 4. Ideal Nyquist plot of IS spectrum of the PV cell

this range, the information of the recombination process can be estimated.

- High frequency range ($f_2 \leq f \leq f_3$): If the IS spectrum of the PV cell can cover this range, the information of both recombination and transportation processes can be revealed.
- Super high frequency range ($f \geq f_3$): A relatively complete IS spectrum can be obtained and all the parameters including the inductance and resistance caused by connection lines can be extracted.

According to the analysis in [22], the boundaries of high and super high frequency ranges are satisfied as: f_2, $f_3 \in [10\ k\text{Hz}\ 100\ k\text{Hz}]$. To obtain the IS spectrum in each frequency range, the bandwidth of the connected converter and sampling devices should be higher than the corresponding frequency of the IS spectrum [38], [39]. However, wide converter bandwidth and high-precision devices would pose great challenges to current technology and increase the overall system cost, which is impractical for small-scale residential applications. Typically, the cost-effective equipment can ensure that the IS spectrum enters the medium frequency range.

In addition, one PV panel typically consists of several PV cells connected in series and parallel to increase its output voltage and current. Its major relaxation processes are the same as those of a PV cell. Generally, to improve the operating efficiency of the PV panel, bypass diodes are connected with a string of PV cells [40]. As an example, for the PV panel applied on our platform (60MXXX of RECOM-SILLIA), one bypass diode is connected in parallel for every 20 cells and there are in total 3 bypass diodes. When the PV panel experiences partial shading or other faulty conditions, bypass diodes will be activated, causing the connected string of PV cells to operate at the short-circuit point. The combined part will primarily exhibit the characteristics of an activated bypass diode. Therefore, the bypass diodes should be considered in the analysis of the impedance of PV panel. Considering the frequency limitation, when the bypass diode is activated, it can be regarded as a resistor, with its value changing according to the trend described in [41]; when it is inactivated, it can be ignored.

By combining all the resistors connected in series, the total series resistance for the AC-ECM at the panel level can be obtained and is symbolized as R_s, as indicated in Fig. 5 (a), where R_{tr} represents the transition resistance; R_{il} represent the resistance caused by the illumination; R_{byd} means the resistance of activated bypass diode, and R_{series} is the resistance resulted by the connection lines, respectively. The recombination process is represented by a sub-circuit, i.e., R_p // C_p. According to the AC-ECM at the panel level, corresponding health features can be defined to reflect its health states.

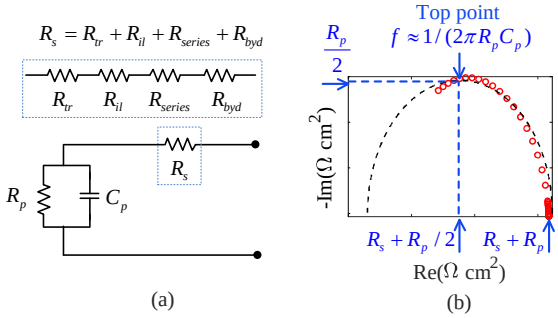

Fig. 5. AC-ECM at the panel level and data analysis: (a) panel-level AC-ECM; (b) Nyquist plot of an experimental IS spectrum and its fitting curve.

B. Health features

The impedance of AC-ECM at the panel level, indicated in Fig. 5 (a), can be calculated by:

$$Z = R_s + R_p//C_p \tag{2}$$

Substituting the impedance of C_p, i.e., $j\omega C_p$, (2) can be replaced by:

$$Z = R_s + \frac{R_p}{1+(\omega R_p C_p)^2} + j\frac{R_p^2 C_p}{1+(\omega R_p C_p)^2} \tag{3}$$

where ω represents the angular frequency and is equal to: $\omega = 2\pi f$ (rad/s).

Hence, the real and imaginary part of the impedance can be separately expressed as:

$$\begin{cases} \text{Re} = R_s + R_p/\left(1+(\omega R_p C_p)^2\right) \\ \text{Im} = R_p^2 C_p/\left(1+(\omega R_p C_p)^2\right) \end{cases} \tag{4}$$

As the frequency increases, the value of Re decreases. The maximum value of Re is equal to $R_s + R_p$, when the frequency approaches 0 Hz. The impedance spectrum reaches its peak when the imaginary part attains its maximum value. At this point, the corresponding frequency, imaginary part, and real part are given by $1/(2\pi R_p C_p)$, $-R_p/2$ and $R_s + R_p/2$, respectively. These two specific points can serve as boundary limitations during curve fitting.

As shown by the red circles in Fig. 5 (b), the measured IS spectrum is incomplete due to the limitation of the converter bandwidth. Considering the boundary constraints, the complete fitted IS spectrum is illustrated by the dashed black line in Fig. 5. The fitting accuracy is evaluated using the normalized root mean square error (NRMSE):

$$\begin{aligned} NRMSE &= \frac{RSME}{(X_{exp,max} - X_{exp,min})} \\ RMSE &= \sqrt{\frac{\sum_{i=1}^{n}(X_{exp} - X_{model})^2}{n}} \end{aligned} \tag{5}$$

where X_{exp} and X_{model} represent the average value of the experimental data and the ideal model values, respectively, as

shown in (4). Additionally, $X_{exp,max}$ and $X_{exp,min}$ denote the maximum and minimum values of X_{exp}, respectively.

Based on the above analysis, the values of R_s, R_p and C_p can be determined. Generally, their value changing trends can be estimated by [42] , as shown in (6):

$$\begin{cases} \ln R_p \propto -qV_{PV}/(m_R kT) \\ \ln C_p \propto qV_{PV}/(m_C kT) \end{cases} \tag{6}$$

where q represents the elementary charge of an electron ($q = 1.6 \times 10^{-19}(C)$; V_{PV} is the DC voltage of the PV panel; T represents the temperature in Kelvin (K); k is the Boltzmann constant ($k = 1.38 \times 10^{-23}$(J/K)); m_C and m_R represent the coefficients related to the ideality factor of the PV panel, and satisfy $m_C < m_R$.

As indicated in (6), both the output voltage and the temperature of the PV panel impact the values of $\ln R_p$ and $\ln C_p$. Since the output voltage is linked to the injection point, which is controlled manually, it is considered as a controlled factor in this work. Additionally, the output voltage of the PV panel and the temperature are coupled [43], when the output current is maintained at a constant value. Thus, a combination of $\ln R_p$, $\ln C_p$ and the output voltage, i.e., V_{PV}, can be used to reflect changes in temperature. However, under illumination, in addition to temperature and output voltage, the value of R_p and C_p are also determined by thermal recombination and total charge, i.e., $R_{th} = m_R kT/Jq$, where J represents the photogenerated current.

Furthermore, the internal conductivity significant influences the efficiency of the PV panel. Under fixed operating conditions, as internal conductivity increases, the output power of the PV panel initially rises and then declines. The maximum output power is achieved When internal conductivity reaches a balance with the conductivity of external load. Internal conductivity can be evaluated using the total resistance, i.e., $R_s + R_p$. The recombination of carriers is influenced by their lifetime and energy levels. To accurately describe the recombination process, the corresponding time constant is required. It can be calculated using R_p and C_p and is denoted as τ.

Therefore, four health features with specific physical meanings are defined, as summarized below:

- **Feature 1, 2: $\ln(R_p)/V_{PV}$, $\ln(C_p)/V_{PV}$**: they contribute to analyzing the influence of temperature and output voltage on the recombination process.
- **Feature 3:** $R_s + R_p$: the equivalent total resistance of the PV panel. It can reflect the conductivity of the PV panel. A smaller value of $R_s + R_p$ indicates better conductivity. On the other hand, increased conductivity is also manifested by a higher internal current of the PV panel, i.e., $I_{sc} - I_{PV}$, where I_{sc} and I_{PV} represent the short-circuit and the output current of the PV panel.
- **Feature 4:** τ: τ represents the time constant of the recombination process and is given by $\tau = R_p C_p$. An increase in carrier energy makes recombination more difficult, leading to a higher value of τ.

These four health features provide valuable insights into the health states of the PV panel under various operating conditions. Before diagnosing the faults, it is essential to characterize the changing trends of these health features across different operating conditions, including both normal and abnormal states. The influence of operating conditions on the health features will be further analyzed in the next section.

IV. Experimental Verification

A. Experimental setup

An experimental platform has been developed in the laboratory, as shown in Fig. 6, with a focus on achieving a transfer efficiency of over 95% and an input current ripple of less than 5%. The platform includes a PV panel (RECOM-SILLIA 60MXXX), a boost converter based on a half-bridge SiC power module (PEB 8024) with an integrated DC bus capacitor (C = 260 uF) and with an inductor (L = 2.5 mH) in series, and a resistive output load (R_L = 96 Ω). The current signal is collected by a high-precision current transducer (IT 65-S ULTRASTAB). The detailed information is listed in Table I. The perturbation signal and the corresponding response signals are generated and collected by a real-time control system (dSPACE SCALEXIO box).

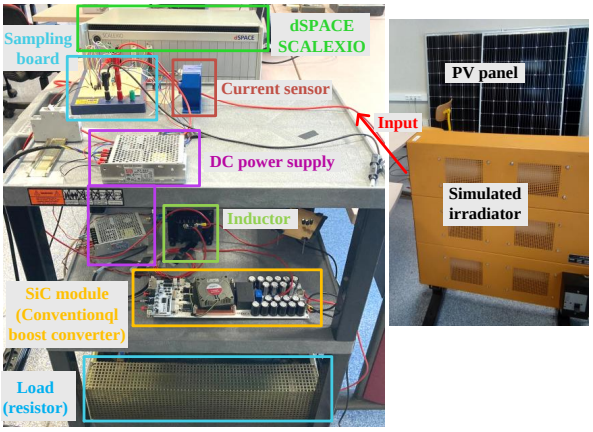

Fig. 6. Experimental platform.

TABLE I
Parameters of Experimental Platform

Part	Description	Symbol	Values
PV panel	Open-circuit voltage	V_{oc}	39.6 V
	Short-circuit current	I_{sc}	9.95 A
	Voltage at MPP	V_{MPP}	32.3 V
	Current at MPP	I_{MPP}	9.56 A
	Standard irradiance	G	1000 W/m^2
	Standard temperature	T	298.15 K
	Size	S	156*156*60 mm^2
Frequency	Switching frequency	f_{sw}	80 kHz
	Sampling frequency	f_{sam}	80 kHz

For the IS implementation, the amplitude of the perturbation signal is set to 15 % of the DC component of the PV current to ensure the linearity criterion and sampling accuracy. The frequency range of the perturbation signal is [1 Hz, 2 kHz]. The number of frequency points per decade is 10 for the frequency range [1 Hz, 1 kHz], and with a frequency increment of 100 Hz in the frequency range [1 kHz, 2 kHz]

to enable a more precise curve fitting in the high frequency range. The number of cycles per frequency is 10 and the number of samples per cycle is at least 40 to ensure accurate representations of the AC waveforms. The total measuring time for one IS measurement is approximately 31.3 s.

To verify the above analysis, experiments are conducted under different temperatures, irradiance levels and partial shading percentages. The corresponding IV curves under the same operating conditions are measured. It is clear that the output power initially increases from 0 W to its maximum value and then gradually decreases back to 0 W. To evaluate the performance of the health features, multiple sets of experimental data are collected under the same conditions, and a 95% confidence interval is applied to ensure the reliability of the results.

B. Influence of different operating temperatures

Temperature is a critical factor influencing the performance of the PV panel. The IV curves at eight different temperatures (ranging from 291.15 K to 232.15 K) under the same irradiance level (250 $\mathrm{W/m^2}$) are shown in Fig. 7 (a). The results indicate that an increase in temperature leads to a decrease in open-circuit voltage. Meanwhile, the short-circuit current exhibits only a slight deviation. When the value of I_{PV} at the injection point is controlled constant, the value of $(I_{sc} - I_{PV})$ also changes slightly, demonstrating that the conductivity is only marginally affected by temperature variations.

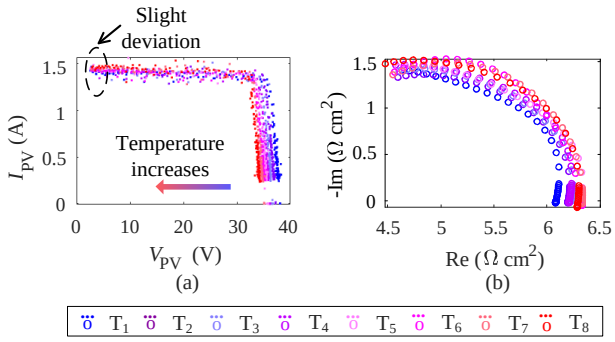

Fig. 7. Experimental results under different temperatures: (a) IV curves; (b) Nyquist curves.

The perturbation signal is injected at I_{PV} = 0.7 A, located in the quasi-linear voltage source region. The impedance information, as described by the Nyquist curves in Fig. 7 (b), exhibits a high degree of consistency. Based on the Nyquist curves, four health features are extracted and illustrated in Fig. 8. (a) and (b) increase with temperature. As analyzed from the IV curves, the slight impact of temperature on I_{sc} means that the conductivity remains nearly unaffected by temperature, as shown in Fig. 8 (c). Additionally, since the output voltage decreases with temperature at the injection point, the carrier energy slightly increases, resulting in minor changes in the recombination time constant, as depicted in Fig. 8 (d).

C. Influence of different irradiance levels

The IV curves under different irradiance levels are shown in Fig. 9 (a), with the irradiance level ranging from 218 $\mathrm{W/m^2}$ to

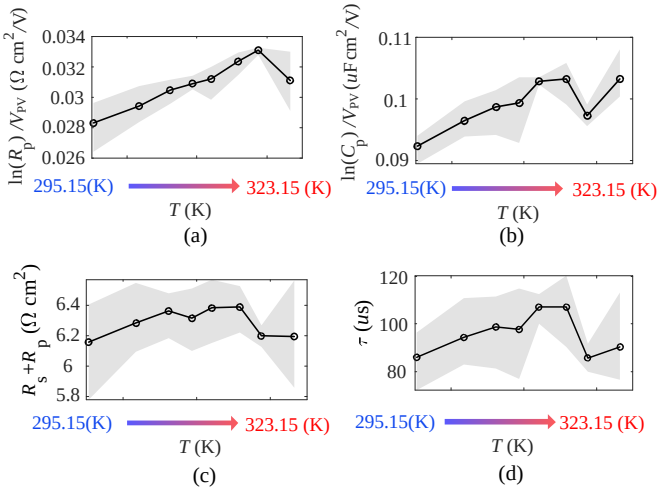

Fig. 8. Health features under different temperatures (with a 95% confidence level in grey): (a) Feature 1; (b) Feature 2; (c) Feature 3; (d) Feature 4.

284 $\mathrm{W/m^2}$. It can be observed that changes in the irradiance level have a significant impact on I_{sc}.

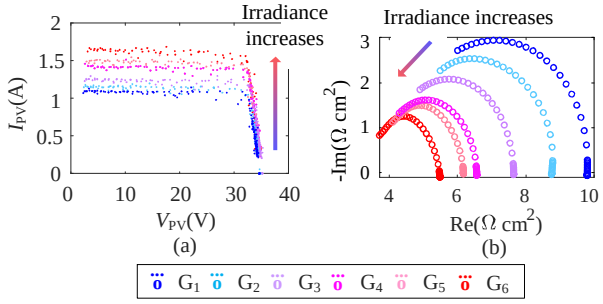

Fig. 9. Experimental results under different irradiance levels: (a) IV curves; (b) Nyquist curves.

The corresponding IS spectra in Nyquist plots for the six irradiance levels, based on the average values, are shown in Fig. 9 (b). Changes in the irradiance level are reflected in the Nyquist curve, which contracts from the upper right to the lower left as the irradiance level increases.

The four health features under different irradiance levels are extracted and depicted in Fig. 10. Fig. 10 (a) and (b) show that as the irradiance level increases, Feature 1 decreases, while Feature 2 exhibits an opposite trend. . In Fig. 10 (c), $R_s + R_p$ decreases with the increase in irradiance level, indicating an increase in the conductivity of the PV panel, consistence with the observations from the IV curves. As the irradiance level increases, carriers gain more energy, leading to an increase in the recombination time constant, as illustrated in Fig. 10 (d).

D. Influence of different partial shading percentages

Partial shading is a comment fault condition encountered during the outdoor operation of PV panels. The PV panel used in this study consists of 60 PV cells arranged in 6 columns. To simulate partial shading conditions, the first column is shaded by a plate at varying percentages (from 0 % to 100 %) and a set of IV curves is obtained, as shown in Fig. 11

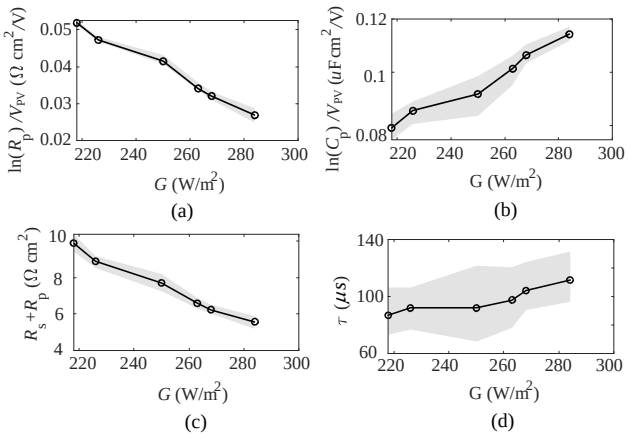

Fig. 10. Health features under different irradiance levels (with a 95% confidence level in grey): (a) Feature 1; (b) Feature 2; (c) Feature 3; (d) Feature 4.

(a). Different partial shading percentages result in a step at different current levels of the IV curves. However, only a complete IV curve allows this step to be clearly observed and utilized to distinguish the occurrence of partial shading. In IS mode, the DC current at the injecting point is set to 0.7 A as other cases, and the PV panel operates under a fixed irradiance level of 284 $\mathrm{W/m^2}$ and at a temperature of 315 K.

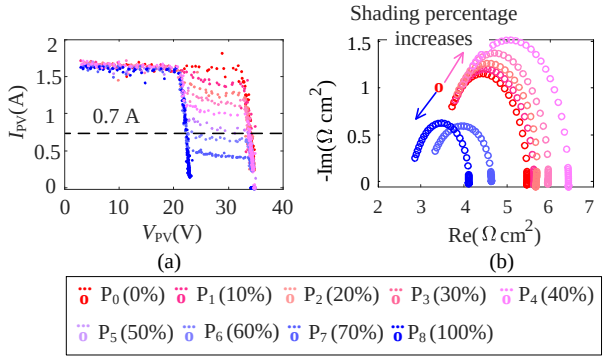

Fig. 11. Experimental results under different partial shading percentages: (a) IV curves; (b) Nyquist curves.

Based on the location of the injection point on the IV curves, the operating conditions under partial shading can be separated into 3 groups.

1) Group 1: this group includes condition $P_0 - P_4$. Under these conditions, the injecting points are located behind the step caused by partial shading.
2) Group 2: this group includes P_5 and P_6. As the shading percentage increases, the IV curve step moves downward, causing the injecting point to appear in a nonlinear region.
3) Group 3: when the injecting points are located in front of the step, the bypass diode is activated during IS test, such as P_7 and P_8.

In both Group 1 and Group 3, the injection points are located in the (quasi-)linear region. However, the injection points in Group 2 fall within the nonlinear region, which is not analyzed in this work. The IS spectra based on average values under Group 1 and Group 3 are depicted in Fig. 11 (b). The result indicate that there is a jump caused by the bypass diode.

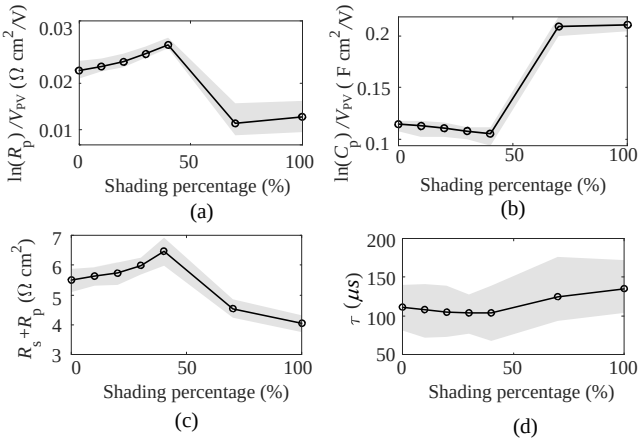

Fig. 12. Health features under different partial shading percentages (with a 95% confidence level in grey): (a) Feature 1; (b) Feature 2; (c) Feature 3; (d) Feature 4.

The four health features are extracted and illustrated in Fig. 12. When the bypass diode is switched off, the health features behave as if the irradiance levels decrease with an increasing shading percentage: the overall conductivity of the PV panel diminishes and the corresponding time constant reduces. Conversely, when the bypass diode is activated, all parameters undergo a sudden change. By bypassing the shaded regions, the conductivity of the PV panel increases, which in turn elongates the recombination time constant.

E. Summary

The experimental results demonstrate that converter-based IS can collect impedance data online and reflect changes in the operating conditions, such as temperatures, irradiance levels and partial shading percentages. When the operating factors increases, the changing trends of the four health features are summarized in Table. II. According to Table. II, Feature 1 and 2 are effective in distinguishing changes in temperature or irradiance level. Feature 3 and 4 can be used to distinguish the effects of irradiance level and partial shading with an activated bypass diode. Even with a relatively limited frequency range, the parameters of the simplified AC-ECM can effectively achieve the health monitoring of the PV panel under different operating conditions.

TABLE II
SUMMARY OF THE HEALTH FEATURES

Health features	T ↑	G ↑	Partial shading percentage ↑	
			bypass diode off	bypass diode on
Feature 1	↑	↓	↑	↑
Feature 2	↑	↑	↓	↑
Feature 3	↑	↓	↑	↓
Feature 4	↑	↑	↓	↑

V. Conclusion

IS is an effective tool for real-time characterization of the internal impedance of PV panels. Unlike traditional IS implementation, which generally require a specially designed workstation, converter-based IS measurement can much facilitate online health monitoring with reduced volume and lower cost. However, the converter bandwidth limits the acquisition of a complete IS spectrum which should achieve at least 100 kHz. This work proposes a simplified AC-ECM at the panel level to facilitate IS implementation via the converter, considering both the limitations of converter bandwidth and the existence of bypass diodes. Four health features are defined based on the proposed AC-ECM and are linked to the internal relaxation processes of the PV panel, providing a more intuitive and reliable basis for further health characterization. Impedance spectra are obtained online under different operating conditions by controlling the connected converter, and the corresponding experimental results demonstrate that the simplified AC-ECM and corresponding analysis methods enable effective health monitoring of the PV panel within a relatively limited frequency range. Future work will focus on analyzing these health features under a broader range of outdoor operating conditions and defective PV panels. Additionally, we aim to develop advanced faults diagnosis and prognostic methods based on the proposed health features to enhance reliability and long-term performance assessment.

References

[1] S. Pourfarrokh, J. Adabi, and F. Zare, "A New Grid-Connected Asymmetrical Multilevel Converter for PV Application," *IEEE Transactions on Power Electronics*, vol. 39, no. 9, pp. 11256–11265, 2024.

[2] X. Wang, Z. Zheng, M. Aillerie, J.-P. Sawicki, A. De Bernardinis, M.-C. Péra, and D. Hissel, "Control Strategies of Converter-Based Online Impedance Spectroscopy for Photovoltaic Panels," *IEEE Transactions on Industry Applications*, pp. 1–15, 2024.

[3] N. Saxena, I. Hussain, B. Singh, and A. L. Vyas, "Implementation of a Grid-Integrated PV-Battery System for Residential and Electrical Vehicle Applications," *IEEE Transactions on Industrial Electronics*, vol. 65, no. 8, pp. 6592–6601, 2018.

[4] European Commission, "EU Solar Energy Strategy," Tech. Rep. 69, 2022.

[5] S. K. Firth, K. J. Lomas, and S. J. Rees, "A simple model of PV system performance and its use in fault detection," *Solar Energy*, vol. 84, no. 4, pp. 624–635, 2010.

[6] S. Lu, B. T. Phung, and D. Zhang, "A comprehensive review on DC arc faults and their diagnosis methods in photovoltaic systems," *Renewable and Sustainable Energy Reviews*, vol. 89, no. March, pp. 88–98, 2018.

[7] Z. Jiang, G. Du, Z. Song, S. Cao, G. Wang, and L. Ma, "Electromagnetic Method for Detecting Black Piece on Monocrystalline Silicon Photovoltaic Panels," *IEEE Transactions on Instrumentation and Measurement*, vol. 73, 2024.

[8] W. Pang, Y. Cui, Y. Zhang, X. Zhang, and H. Yan, "Comparisons of photovoltaic modules for their performances based on different substrates," *Applied Thermal Engineering*, vol. 146, pp. 505–514, 2019.

[9] B. Yang, R. Zheng, Y. Han, J. Huang, M. Li, H. Shu, S. Su, and Z. Guo, "Recent Advances in Fault Diagnosis Techniques for Photovoltaic Systems: A Critical Review," *Protection and Control of Modern Power Systems*, vol. 9, no. 3, pp. 36–59, 2024.

[10] R. Singh, V. K. Yadav, and M. Singh, "An Improved Hot Spot Mitigation Approach for Photovoltaic Modules Under Mismatch Conditions," *IEEE Transactions on Industrial Electronics*, vol. 71, no. 5, pp. 4840–4850, 2024.

[11] D. A. R. Barkhouse, O. Gunawan, T. Gokmen, T. K. Todorov, and D. B. Mitzi, "On the detection of shunts in silicon solar cells by photo and electroluminescence imaging," *Progress in Photovoltaics: Research and Applications*, vol. 20, no. 1, pp. 6–11, 2015.

[12] G. M. El-Banby, N. M. Moawad, B. A. Abouzalm, W. F. Abouzaid, and E. A. Ramadan, "Photovoltaic system fault detection techniques: a review," *Neural Computing and Applications*, vol. 35, no. 35, pp. 24829–24842, 2023.

[13] R. Duru, D. Le Cunff, M. Cannac, I. Mica, J. Baruchel, T. N. Tran-Thi, and G. Bremond, "Photoluminescence Imaging for Buried Defects Detection in Silicon: Assessment and Use-Cases," *IEEE Transactions on Semiconductor Manufacturing*, vol. 32, no. 1, pp. 23–30, 2019.

[14] A. Eskandari, J. Milimonfared, and M. Aghaei, "Fault Detection and Classification for Photovoltaic Systems Based on Hierarchical Classification and Machine Learning Technique," *IEEE Transactions on Industrial Electronics*, vol. 68, no. 12, pp. 12750–12759, 2021.

[15] X. Wang, Z. Zheng, M. Aillerie, A. De Bernardinis, J. P. Sawicki, M. C. Péra, and D. Hissel, "Cooperative Control of Online Impedance Spectroscopy Monitoring Method and Maximum Power Point Tracking Method for Photovoltaic Panels," in *24th European Conference on Power Electronics and Applications, EPE 2022 ECCE Europe*, 2022.

[16] J. Lv, J. Kuang, Z. Yu, G. Sun, J. Liu, and J. I. Leon, "Diagnosis of PEM Fuel Cell System Based on Electrochemical Impedance Spectroscopy and Deep Learning Method," *IEEE Transactions on Industrial Electronics*, vol. 71, no. 1, pp. 657–666, 2024.

[17] P. Jiang, J. Chen, L. Jin, and L. Kumar, "Adaptive Condition Monitoring for Fuel Cells Based on Fast EIS and Two-Frequency Impedance Measurements," *IEEE Transactions on Industrial Electronics*, vol. 70, no. 8, pp. 8517–8525, 2023.

[18] J. Zuo, N. Y. Steiner, Z. Li, and D. Hissel, "Quantitative investigation of internal polarization in a proton exchange membrane water electrolyzer stack using distribution of relaxation times," *Applied Energy*, vol. 386, p. 125543, 2025.

[19] J. Zuo, N. Y. Steiner, Z. Li, and D. Hissel, "Degradation root cause analysis of pem fuel cells using distribution of relaxation times," *Applied Energy*, vol. 378, p. 124762, 2025.

[20] C. Gonzales, A. Guerrero, and J. Bisquert, "Transition from Capacitive to Inductive Hysteresis: A Neuron-Style Model to Correlate I- V Curves to Impedances of Metal Halide Perovskites," *Journal of Physical Chemistry C*, vol. 126, no. 32, pp. 13560–13578, 2022.

[21] T. Yeow, J. Sun, Z. Yao, J.-n. Jaubert, and K. P. Musselman, "Evaluation of impedance spectroscopy as a tool to characterize degradation mechanisms in silicon photovoltaics," *Solar Energy*, vol. 184, no. March, pp. 52–58, 2019.

[22] J. Panigrahi, A. Pandey, S. Bhattacharya, A. Pal, S. Mandal, and V. Krishna Komarala, "Impedance spectroscopy of amorphous/crystalline silicon heterojunction solar cells under dark and illumination," *Solar Energy*, vol. 259, no. May, pp. 165–173, 2023.

[23] O. Almora and G. Garcia-Belmonte, "Light capacitances in silicon and perovskite solar cells," *Solar Energy*, vol. 189, no. July, pp. 103–110, 2019.

[24] N. Katayama, S. Osawa, S. Matsumoto, T. Nakano, and M. Sugiyama, "Degradation and fault diagnosis of photovoltaic cells using impedance spectroscopy," *Solar Energy Materials and Solar Cells*, vol. 194, no. February, pp. 130–136, 2019.

[25] A. Geng, H. Hu, Y. Peng, Z. Zhao, Z. He, and S. Gao, "Wideband Measurement Approach for EIS of Lithium-Ion Batteries Using Low-Frequency Concentrated Disturbance," *IEEE Transactions on Industrial Electronics*, vol. 71, no. 5, pp. 4851–4860, 2024.

[26] X. Wang, X. Wei, Q. Chen, and H. Dai, "A Novel System for Measuring Alternating Current Impedance Spectra of Series-Connected Lithium-Ion Batteries with a High-Power Dual Active Bridge Converter and Distributed Sampling Units," *IEEE Transactions on Industrial Electronics*, vol. 68, no. 8, pp. 7380–7390, 2021.

[27] J. A. A. Qahouq, S. Member, Z. Xia, and S. Member, "Single-Perturbation-Cycle Online Battery Impedance Spectrum Measurement Method With Closed-Loop Control of Power Converter," *IEEE Transactions on Industrial Electronics*, vol. 64, no. 9, pp. 7019–7029, 2017.

[28] "Robust voltage control of bidirectional dc-dc converter with modified extended state observer for hybrid power supply system,"

[29] "Online internal temperature estimation for lithium-ion batteries using the suppressed second-harmonic current in single-phase dc/ac converters,"

[30] R. M. Pujahari, *Crystalline silicon solar cells*. Springer, 2021.

[31] J. E. Garland, D. J. Crain, J. P. Zheng, C. M. Sulyma, and D. Roy, "Electro-analytical characterization of photovoltaic cells by combining voltammetry and impedance spectroscopy: Voltage dependent parameters of a silicon solar cell under controlled illumination and temperature," *Energy and Environmental Science*, vol. 4, no. 2, pp. 485–498, 2011.

[32] D. A. van Nijen, M. Muttillo, R. Van Dyck, J. Poortmans, M. Zeman, O. Isabella, and P. Manganiello, "Revealing capacitive and inductive

effects in modern industrial c-Si photovoltaic cells through impedance spectroscopy," *Solar Energy Materials and Solar Cells*, vol. 260, no. April, p. 112486, 2023.
[33] M. M. Shehata, T. N. Truong, R. Basnet, H. T. Nguyen, D. H. Macdonald, and L. E. Black, "Impedance spectroscopy characterization of c-Si solar cells with SiOx/ Poly-Si rear passivating contacts," *Solar Energy Materials and Solar Cells*, vol. 251, p. 112167, 2023.
[34] K. A. Kim, C. Xu, L. Jin, and P. T. Krein, "A dynamic photovoltaic model incorporating capacitive and reverse-bias characteristics," *IEEE Journal of Photovoltaics*, vol. 3, no. 4, pp. 1334–1341, 2013.
[35] K. A. Kim, G. S. Seo, B. H. Cho, and P. T. Krein, "Photovoltaic Hot-Spot Detection for Solar Panel Substrings Using AC Parameter Characterization," *IEEE Transactions on Power Electronics*, vol. 31, no. 2, pp. 1121–1130, 2016.
[36] E. Von Hauff, "Impedance Spectroscopy for Emerging Photovoltaics," *Journal of Physical Chemistry C*, vol. 123, no. 18, pp. 11329–11346, 2019.
[37] I. Mora-Seró, Y. Luo, G. Garcia-Belmonte, J. Bisquert, D. Muñoz, C. Voz, J. Puigdollers, and R. Alcubilla, "Recombination rates in heterojunction silicon solar cells analyzed by impedance spectroscopy at forward bias and under illumination," *Solar Energy Materials and Solar Cells*, vol. 92, no. 4, pp. 505–509, 2008.
[38] E. R. da Silva and M. E. Elbuluk, *Fundamentals of Power Electronics*, vol. 59. New York, NY, USA: Springer, 2020.
[39] O. I. Olayiwola and P. S. Barendse, "Dynamic equivalent circuit modelling of polycrystalline silicon photovoltaic cells," *2017 IEEE Energy Conversion Congress and Exposition, ECCE 2017*, vol. 2017-Janua, pp. 2310–2317, 2017.
[40] M. Dhimish and Z. Chen, "Novel Open-Circuit Photovoltaic Bypass Diode Fault Detection Algorithm," *IEEE Journal of Photovoltaics*, vol. 9, no. 6, pp. 1819–1827, 2019.
[41] C. Y. L. hui and L. Xiangwei, "Study of bypass diodes configuration on PV modules with partial shaded," in *2019 Chinese Control And Decision Conference (CCDC)*, (Nanchang, China), pp. 511–515, 2019.
[42] O. Almora, Y. Zhao, X. Du, T. Heumueller, G. J. Matt, G. Garcia-Belmonte, and C. J. Brabec, "Light intensity modulated impedance spectroscopy (LIMIS) in all-solid-state solar cells at open-circuit," *Nano Energy*, vol. 75, no. November 2019, 2020.
[43] Z. Zhang, M. Ma, H. Wang, H. Wang, W. Ma, and X. Zhang, "A fault diagnosis method for photovoltaic module current mismatch based on numerical analysis and statistics," *Solar Energy*, vol. 225, no. April, pp. 221–236, 2021.

Xin Wang (Student Member, IEEE) is a Postdoctoral Research Associate with the FEMTO-ST (CNRS) Institute of University of Franche-Comté (Université Marie et Louis Pasteur since January 2025), France. In 2024, She received the Ph.D. degree in University of Lorraine, Metz, France. She received the B.S and M.S degrees in Electrical Engineering from Beijing Jiaotong University, Beijing, China, in 2017 and 2020, respectively. Her research interests include fault diagnosis and control of AC/DC and DC/DC converters in DC microgrid applications.

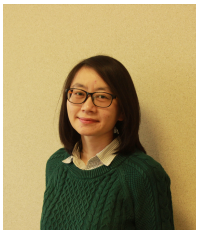

Zhixue Zheng (S'13–M'18) is an Associate Professor with the FEMTO-ST (CNRS) Institute of University of Franche-Comté (Université Marie et Louis Pasteur since January 2025), Belfort, France, since September 2024. From 2018 to 2024, she has worked with the laboratory LMOPS, University of Lorraine and CentraleSupélec, Metz, France. She received her bachelor's degree and master's degree in Electrical Engineering from Beijing Jiaotong University in 2009, and Tsinghua University in 2011 respectively. In 2014, She received the Ph.D. degree from the University of Franche-Comté. Her research interests include diagnostic and prognostic of hydrogen energy systems, as well as energy and health management of DC microgrids.

Michel Aillerie obtained a PhD in 1991 and the Habilitation to Lead Researches in 2001 at the Université Paul Verlaine of Metz, currently Université de Lorraine. He is a Full Professor since 2005 and conducts his research in the city of Metz at the Laboratoire Materiaux Optiques et Photonique (LMOPS), a joint laboratory of the University of Lorraine and CentraleSupélec, France. His interests and activities concern two main themes. The first one concerns the characterization of functional non-linear optical properties of materials for optoelectronic applications. The second one concerns the development and optimization of energy production and management systems in a sustainable development approach.

Marie-Cécile Péra is a Full Professor at the University of Franche-Comté (Université Marie et Louis Pasteur since January 2025), France. From 2008 to 2012, she was the Deputy Head of the Energy Department of FEMTO-ST. From 2012 to 2019, she was the deputy Director of the FEMTO-ST Institute (800 persons). Since 2020, she's the director of the technical and scientific resource center FCLAB on hydrogen systems. She is a member of the French National Council of CNRS (Section 08). She works on energy management of hybrid electric power generation systems (fuel cells, PEMFC and SOFC, supercapacitors, batteries), the control, diagnosis and prognostics of fuel cell systems.

Daniel Hissel is a Full Professor at the University of Franche-Comté (Université Marie et Louis Pasteur since January 2025), France. Since 2012, he is the Head of the "Hydrogen-energy systems, production, storage, and conversion of electricity" research team at the FEMTO-ST (CNRS) Institute. His main research activities revolve around hydrogen systems dedicated to automotive and stationary applications, modeling, non-linear control and energy optimization of these systems and diagnostic/prognostic. Since 2020, he is also the Deputy Director of the French national hydrogen research federation (CNRS), gathering about 300 researchers on hydrogen technologies in France. For his work towards industrialisation of hydrogen systems, he has obtained in 2017 the Blondel Medal of the SEE, and in 2020 the Innovation Medal of the CNRS. He is a Fellow of IEEE since 2021, and holds a senior innovation chair at the Institut Universitaire de France (IUF) since 2022.